

List-Mode PET Image Reconstruction Using Deep Image Prior

Kibo Ote, Fumio Hashimoto, Yuya Onishi, Takashi Isobe, and Yasuomi Ouchi

Abstract—List-mode positron emission tomography (PET) image reconstruction is an important tool for PET scanners with many lines-of-response (LORs) and additional information such as time-of-flight and depth-of-interaction. Deep learning is one possible solution to enhance the quality of PET image reconstruction. However, the application of deep learning techniques to list-mode PET image reconstruction have not been progressed because list data is a sequence of bit codes and unsuitable for processing by convolutional neural networks (CNN). In this study, we propose a novel list-mode PET image reconstruction method using an unsupervised CNN called deep image prior (DIP) and a framework of alternating direction method of multipliers. The proposed list-mode DIP reconstruction (LM-DIPRecon) method alternatively iterates regularized list-mode dynamic row action maximum likelihood algorithm (LM-DRAMA) and magnetic resonance imaging conditioned DIP (MR-DIP). We evaluated LM-DIPRecon using both simulation and clinical data, and it achieved sharper images and better tradeoff curves between contrast and noise than the LM-DRAMA and MR-DIP. These results indicated that the LM-DIPRecon is useful for quantitative PET imaging with limited events. In addition, as list data has finer temporal information than dynamic sinograms, list-mode deep image prior reconstruction is expected to be useful for 4D PET imaging and motion correction.

Index Terms—Deep neural network, image reconstruction, list-mode, positron emission tomography, unsupervised learning.

I. INTRODUCTION

POSITRON emission tomography (PET) is an in-vivo imaging tool with a wide range of clinical applications such as oncology, cardiology, and neurology [1]. In PET scan, firstly a radiotracer is injected into a subject. Then, the radiotracer emits a positron and an annihilation between positron and electron generates two 511 keV gamma rays. The PET detector ring catches two gamma rays as a coincidence event, i.e., the two annihilation photons (or gamma rays) are detected within a time coincidence window. The coincidence event indicates that an activity is on the line-of-response (LOR), but it cannot be determined where the activity is on the LOR. Hence, an image reconstruction process is needed for tomographic imaging.

Positron emission tomography image reconstruction is a challenging task because the number of events is limited, and it is also an ill-posed inverse problem. Regularization using prior information about PET images is often used to suppress the ill-posedness and statistical noise. For example, the spatial smoothness of an image is used to regularize the PET image

reconstruction through Gibbs priors [2], [3]. In addition, anatomical information from X-ray computational tomography (CT) or magnetic resonance imaging (MRI) can be used for edge-preserving regularization of PET image reconstruction [4]-[6]. Besides these conventional algorithms, some deep learning-based approaches have recently been proposed for PET image reconstruction and provide excellent performance [7]-[10].

One strategy of deep learning-based PET image reconstruction is to learn the image reconstruction from sinograms through large amounts of training datasets [11], [12]. For example, [13] proposed DeepPET, which performs a direct mapping from a sinogram space into reconstructed image space, using a fully convolutional neural network (CNN). It is easy to handle with CNN because the direct mapping process is an image-to-image relationship. In another strategy, [14] proposed a regularization method that uses a CNN representation as prior information. However, these deep learning-based methods still require large amounts of datasets for network training. In recent years, unsupervised learning has attracted attention for PET image reconstruction, especially deep image prior (DIP) [15], which uses the CNN architecture itself as a regularization, is used as a new regularization tool for PET image reconstruction because it requires no prior training data [16]-[18]. However, the number of bins of a sinogram is dependent on the number of LORs, and further increases in orders of magnitude if the PET scanner has the ability to measure additional information, such as time-of-flight (TOF) and depth-of-interaction (DOI). Hence, the sinogram-mode PET image reconstruction becomes memory intensive and sometimes infeasible, when the PET scanner has many LORs and additional information.

List-mode PET image reconstruction is the promising solution for TOF- and DOI-PET image reconstruction when the number of events is less than the number of LORs. In addition, the list-mode method is efficient for dynamic PET image reconstruction because the number of events per frame becomes low [19] and is suitable for motion correction because the list data holds fine temporal information. Hence, improving the list-mode PET image reconstruction is important for advanced PET scanners. However, the incorporation of deep learning techniques to list-mode PET image reconstruction has not advanced because list data is a sequence of bit codes and is not suitable for processing by CNNs.

K. Ote, F. Hashimoto, Y. Onishi, T. Isobe are with Central Research Laboratory, Hamamatsu Photonics K. K., 5000 Hirakuchi, Hamakita-ku, Hamamatsu 434-8601, Japan. (e-mail: kibou@crl.hpk.co.jp, fumio.hashimoto@crl.hpk.co.jp, yuya.onishi@crl.hpk.co.jp, isobe-t@crl.hpk.co.jp).

Y. Ouchi is with Department of Biofunctional Imaging, Preeminent Medical Photonics Education & Research Center, Hamamatsu University School of Medicine, 1-20-1 Handayama, Higashi-ku, Hamamatsu 431-3192, Japan. (e-mail: ouchi@hama-med.ac.jp).

To surpass the above barriers, in this study, we propose list-mode PET image reconstruction using DIP. The proposed method, called LM-DIPRecon, alternatively iterates list-mode PET image reconstruction and image processing by DIP, according to an alternating direction method of multipliers (ADMM) [20]. We evaluated the proposed LM-DIPRecon method using Monte-Carlo simulation and clinical data. The LM-DIPRecon method reduces noise and maintains the contrast compared with post-processing by the DIP method.

II. RELATED WORKS

In this section, we introduce list-mode PET image reconstruction and DIP.

A. List-mode PET image reconstruction

The list data is formulated as,

$$U = \{i(t) | t = 1, 2, \dots, T\}, \quad (1)$$

where t is an index of a coincidence event, T is the number of events, and $i(t)$ is an index of LOR measuring the t -th event.

The list-mode log-likelihood function [21] is defined as,

$$L(U|x) = \sum_t \log \sum_j a_{i(t)j} x_j - \sum_i \sum_j a_{ij} x_j, \quad (2)$$

where x is an unknown image, j is an index of a voxel, and a_{ij} represents the contribution of the voxel j to the LOR i .

We can reconstruct the image from the list data by maximizing the list-mode log-likelihood function with an iterative algorithm. For fast global optimization, the list-mode dynamic row action maximum likelihood algorithm (LM-DRAMA) has been developed [22], [23]. The reconstructed image x_{EM} is calculated using LM-DRAMA updates, as follows:

$$x_{j,EM}^{(k,q+1)} = x_j^{(k,q)} + x_j^{(k,q)} \lambda^{(k,q)} \left(\frac{N_{sub}}{S_j} \sum_{t \in Sub_q} \frac{a_{i(t)j}}{y_i^{(k,q)}} - 1 \right), \quad (3)$$

$$S_j = \sum_i a_{ij}, \quad (4)$$

$$y_i^{(k,q)} = \sum_j a_{ij} x_j^{(k,q)}, \quad (5)$$

$$\lambda^{(k,q)} = \frac{\beta}{\beta + q + \gamma k N_{sub}}, \quad (6)$$

where k is the number of main iteration, q is the number of sub-iteration, N_{sub} is the number of subsets of list data, S is the sensitivity image [24], y is the forward projection of the image, λ is a subset-dependent relaxation coefficient, Sub_q is a subset of list data accessed at the q -th sub-iteration, β and γ are the parameters of the relaxation coefficient.

B. DIP

Deep image prior is an unsupervised deep learning technique for image restoration, and requires no prior training data other than the image itself [15]. The DIP method trains a CNN to map

a prior distribution image to a measured degraded image. When there are no prior information, DIP inputs a random image noise to the CNN as the prior distribution image. CNNs have the property of restoring signals faster than noise, called an inductive bias [15]. By stopping the training early, we can obtain a restored image as an output of the CNN.

The DIP method is formulated as,

$$\operatorname{argmin}_{\theta} \|f_{\theta}(z) - x_{label}\|^2, \quad (7)$$

where f is a CNN, θ is a parameter of the CNN such as the connection weight, z is a prior distribution image, and x_{label} is a measured degraded image.

In addition to the network architecture, the prior distribution image is the key factor that decides the performance of the DIP. For example, if we use CT or MRI as the prior information [25], the recovery of PET images by DIP becomes faster and more accurate than the case of no prior information. For dynamic PET image denoising, we can also use the static PET image as the prior information [26].

III. METHODOLOGY

In this section, we integrate list-mode PET image reconstruction and DIP into one algorithm using ADMM.

A. Integration of LM-DRAMA and DIP

To regularize list-mode PET image reconstruction using DIP, we consider the following constrained optimization problem.

$$\begin{aligned} \max & \quad L(U|x), \\ \text{s. t.} & \quad x = f_{\theta}(z), \end{aligned} \quad (8)$$

where the unknown image x is constrained to the output of the CNN.

The constrained optimization problem in (8) can be rewritten by the augmented Lagrangian method.

$$\min -L(U|x) + \frac{\rho}{2} \|x - f_{\theta}(z) + \mu\|^2 + \frac{\rho}{2} \|\mu\|^2, \quad (9)$$

where ρ is a positive constant and μ is a dual variable.

The ADMM splits the optimization problem of (9) into the two subproblems and the update of dual variable [20].

$$x^{(n+1)} = \operatorname{argmax}_x L(U|x) - \frac{\rho}{2} \|x - f_{\theta}^{(n)}(z) + \mu^{(n)}\|^2, \quad (10)$$

$$\theta^{(n+1)} = \operatorname{argmin}_{\theta} \|f_{\theta}(z) - x^{(n+1)} - \mu^{(n)}\|^2, \quad (11)$$

$$\mu^{(n+1)} = \mu^{(n)} + x^{(n+1)} - f_{\theta}^{(n+1)}(z), \quad (12)$$

where n is the number of iterations of three steps of the ADMM.

B. Solving subproblem (10)

The subproblem (10) can be solved by the optimization transfer method [16], [27], [28]. Firstly, to optimize each voxel independently, we construct the surrogate function of $L(U|x)$ as,

$$Q_L(x|x^{(n)}) = \sum_j S_j(x_{j,EM}^{(n+1)} \log x_j - x_j). \quad (13)$$

The $Q_L(x|x^{(n)})$ will suffice the following two conditions from the convergence property of the DRAMA [29].

$$Q_L(x|x^{(n)}) - Q_L(x^{(n)}|x^{(n)}) \leq L(U|x) - L(U|x^{(n)}), \quad (14)$$

$$\nabla Q_L(x^{(n)}|x^{(n)}) = \nabla L(U|x^{(n)}). \quad (15)$$

By replacing the $L(U|x)$ with the surrogate function $Q_L(x|x^{(n)})$, we obtain the surrogate objective function of subproblem (10) as,

$$P(x_j|x^{(n)}) = S_j(x_{j,EM}^{(n+1)} \log x_j - x_j) - \frac{\rho}{2} (x_j - x_{j,base}^{(n)})^2, \quad (16)$$

$$x_{j,base}^{(n)} = f_{\theta^{(n)}}(z)_j - \mu_j^{(n)}, \quad (17)$$

where x_{base} is a base image of the regularization.

The surrogate objective function (16) can be optimized voxel by voxel. Hence, by setting the derivative of equation (16) to be zero, we can obtain the following update equation.

$$x_j^{(n+1)} = \frac{x_{j,base}^{(n)} - \frac{S_j}{\rho} + \sqrt{\left(x_{j,base}^{(n)} - \frac{S_j}{\rho}\right)^2 + 4x_{j,EM}^{(n+1)} \frac{S_j}{\rho}}}{2}. \quad (18)$$

As a consequence, the algorithm of subproblem (10) becomes a combination of LM-DRAMA and regularization by equation (18).

In this study, we set $N_{sub} = 40$, $\beta = 30$, $\gamma = 0.1$ for the LM-DRAMA. In addition, we set $\rho = 0.5$ for the regularization.

C. Solving subproblem (11)

Subproblem (11) can be solved by the DIP with $x_{label} = x^{(n+1)} + \mu^{(n)}$. In this study, we employ the MR-DIP which uses the MR image as the prior distribution image. In addition, we use the 3D U-net architecture [30] for the MR-DIP because it is suitable for medical image processing, and it may have a good

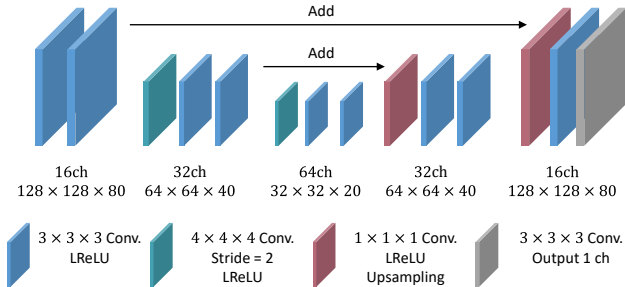


Fig. 1. Network architecture of 3D U-net in this study.

inductive bias for the PET image. Fig 1 shows the network architecture of the 3D U-net in this study. The 3D U-net consists of encoder, decoder, and skip connections.

The encoder extracts the feature maps to generate the PET image from the MR image. The combination of 3D convolution with a kernel size of 3 and a leaky rectified linear unit (LReLU)

is repeated twice before down-sampling. Down-sampling is performed by the combination of 3D convolution with kernel size of 4 and stride of 2 and LReLU. At each down-sampling, the number of channels is doubled.

The decoder reconstructs the PET image from the extracted feature maps. The combination of 3D convolution with kernel size of 3 and LReLU is repeated twice before up-sampling. Up-sampling is performed by the 3D convolution with kernel size of 1 and LReLU and trilinear interpolation. At each down-sampling, the number of channels is halved. The output image is reconstructed by 3D convolution with kernel size of 3 with a single channel output.

The skip connection adds the feature maps before down-sampling to the feature maps before up-sampling by bypassing as shown in Fig. 1.

To stabilize the training, we clip the gradient norm at 1.0 [31] and take an exponential moving average (EMA) of the network output [15] as,

$$EMA = \eta EMA + (1 - \eta) f_{\theta}(z), \quad (19)$$

where η is a smoothing constant. In this study, we set $\eta = 0.99$.

Algorithm 1 Algorithm of the LM-DIPRecon method

Input: Iteration number N , Sub-iteration numbers M_1 and M_2 , Initial network $\theta^{(0)}$, MR image z , positive constant ρ

- 1: $x^{(0)} = f_{\theta^{(0)}}(z)$
- 2: $\mu^{(0)} = \mathbf{0}$
- 3: **for** $n = 0$ **to** $N - 1$ **do**
- 4: $x^{(n,0)} = x^{(n)}$
- 5: $x_{base} = f_{\theta^{(n)}}(z) - \mu^{(n)}$
- 6: **for** $m = 0$ **to** $M_1 - 1$ **do**
- 7: $u = nM_1 + m$
- 8: $k = \lceil u/N_{sub} \rceil$ where $\lceil \cdot \rceil$ is round down.
- 9: $q = u \% N_{sub}$
- 10: $\lambda = \frac{\beta}{\beta + q + \gamma k N_{sub}}$
- 11: $x_{j,EM} = x_j^{(n,m)} + x_j^{(n,m)} \lambda \left(\frac{N_{sub}}{S_j} \sum_{t \in Sub_q} \frac{a_{i(t)} j}{y_{i(t)}^{(n,m)}} - 1 \right)$
- 12: $x_j^{(n,m+1)} = \frac{x_{j,base} - \frac{S_j}{\rho} + \sqrt{\left(x_{j,base} - \frac{S_j}{\rho}\right)^2 + 4x_{j,EM} \frac{S_j}{\rho}}}{2}$
- 13: **end for**
- 14: $x^{(n+1)} = x^{(n,M_1-1)}$
- 15: $x_{label} = x^{(n+1)} + \mu^{(n)}$
- 16: Running L-BFGS method with M_2 iterations to get $\theta^{(n+1)} = \operatorname{argmin}_{\theta} \|f_{\theta}(z) - x_{label}\|^2$
- 17: $\mu^{(n+1)} = \mu^{(n)} + x^{(n,M_1-1)} - f_{\theta^{(n+1)}}(z)$
- 18: **end for**
- 19: **return** $\hat{x} = f_{\theta^{(N-1)}}(z)$

D. Overall algorithm

The overall algorithm of the LM-DIPRecon method is shown in Algorithm 1.

To ready the initial network $\theta^{(0)}$, we take a two-step approach [16]. At first, we reconstruct the image with one main-iteration of the LM-DRAMA and perform the MR-DIP as,

$$\theta^{(0)} = \underset{\theta}{\operatorname{argmin}} \|f_{\theta}(z) - x_{\text{EM}}^{(1)}\|^2. \quad (20)$$

In this step, we update the network parameters by Adam method [32] with 1000 epochs.

In the second step, we iterate the three steps of the ADMM as shown in Algorithm 1. In each step of the ADMM, we have not to solve the subproblems until convergence. At solving subproblem (10), we set $M_1 = 2$ and perform two sub-iterations of the regularized LM-DRAMA. At solving subproblem (11), we set $M_2 = 10$ and update the network parameters using the limited memory Broyden-Fletcher-Goldfarb-Shanno (L-BFGS) method with 10 epochs and a learning rate of 0.1. As the L-BFGS method has a fast convergence rate when the parameters are near a local optimum, we use the Adam method in the first step and the L-BFGS method in the second step.

Lastly, after N iterations, the algorithm outputs the image as,

$$\hat{x} = f_{\theta^{(N-1)}}(z), \quad (21)$$

where \hat{x} is a final image.

IV. EXPERIMENTAL SETUP

We evaluated the proposed methods using the simulation data and clinical data. We compared the proposed method relative to the LM-DRAMA and the MR-DIP. Image size was $128 \times 128 \times 80$ and voxel size was $2.6 \text{ mm} \times 2.6 \text{ mm} \times 2.4 \text{ mm}$. The details of the data correction can be seen in the Appendix.

A. Simulation data

We performed Monte-Carlo simulation using our simulator. We made a digital brain phantom from segmented MR image downloaded from the BrainWeb [33]. The digital brain phantom was set to a contrast of 1.00:0.25:0.05 for gray matter (GM), white matter (WM) and CSF. In addition, we inserted the three tumor regions with a contrast of 1.0, 1.1, and 1.2. Attenuation coefficients were set to 0.00958 mm^{-1} for the soft tissue and 0.0151 mm^{-1} for the bone tissue.

The detector arrangement was same as our brain PET scanner (Hamamatsu HITS-655000 [34]) with four-layer DOI. The simulation included attenuation and scatter. We set the energy window of 400-650 keV with an energy resolution of 15%. The list data had 1.52×10^8 events. To evaluate the denoising performance, we thinned the list data into $1/20$, 7×10^6 events.

The MR image was interpolated to the same dimension of the PET image and used as the prior distribution image of the DIP.

B. Clinical data

A clinical study was performed at Hamamatsu University School of Medicine. The Ethics Committees of Hamamatsu University School of Medicine approved the study, written informed consent was obtained from the participant prior to enrollment. A healthy volunteer was scanned using HITS-655000 for 62 min after injection of 5 MBq/kg of ^{11}C -MeQAA, a tracer for $\alpha 7$ nicotinic acetylcholine receptors [35].

We separated the list data into three frames of 0-20 min, 20-42 min, and 42-62 min. We used the 42-62 min frame to evaluate the uptake of the QAA in the thalamus. The list data of 42-62 min had 4.7×10^7 events. Furthermore, to evaluate the

denoising performance, we thinned the list data into $1/10$, 4.7×10^6 events.

The MRI scan was performed using a 1.5 T MR scanner (Signa HDxt, GE, USA) with the following acquisition parameters: 3D mode sampling, Repetition Time/Time to Echo (TR/TE) (25/Minimum, T1-weighted), 30° flip angle, 1.5 mm slice thickness with no gap, and 256×256 matrices. The MR image was interpolated and aligned to the PET image.

C. Evaluation metrics

In the simulation study, we evaluated the peak signal-to-noise ratio (PSNR) for quantitative evaluation.

$$\text{PSNR} = 10 \log_{10} \frac{\max(x_{\text{ref}})^2}{\frac{1}{N_R} \sum_{j \in R} (x_j - x_{j,\text{ref}})^2}, \quad (22)$$

where x_{ref} is a phantom image, R is a region of the whole brain, and N_R is a number of voxels inside the whole brain.

For tumor quantification, the tumor contrast recovery (CR) was calculated as,

$$\text{CR} = \frac{1}{N_{\text{tumor}}} \sum_{j \in R_{\text{tumor}}} \frac{x_j}{x_{j,\text{ref}}}, \quad (23)$$

where R_{tumor} is a union of the three tumor regions and N_{tumor} is a number of voxels inside the tumor regions.

In addition, we evaluated the curves of contrast recovery coefficient (CRC) versus standard deviation (STD) to evaluate the tradeoff between contrast and noise. The CRC was calculated by the following equations.

$$\text{CRC} = \left(\frac{\bar{a}}{\bar{b}} - 1 \right) / \left(\frac{\bar{a}_{\text{ref}}}{\bar{b}_{\text{ref}}} - 1 \right), \quad (24)$$

$$\bar{a} = \frac{1}{K_a} \sum_{k=1}^{K_a} a_k, \quad (25)$$

$$\bar{b} = \frac{1}{K_b} \sum_{k=1}^{K_b} b_k, \quad (26)$$

where \bar{a} is the average of multiple region of interest (ROI) uptakes set to GM and tumor, \bar{b} is the average of multiple ROI values set to WM, K_a is the number of ROIs on the GM and tumor, K_b is the number of ROIs on WM, a is an ROI uptake on the GM and tumor, b is an ROI value on the WM.

$$a_k = \frac{1}{N_{a,k}} \sum_{j \in R_{a,k}} x_j, \quad (27)$$

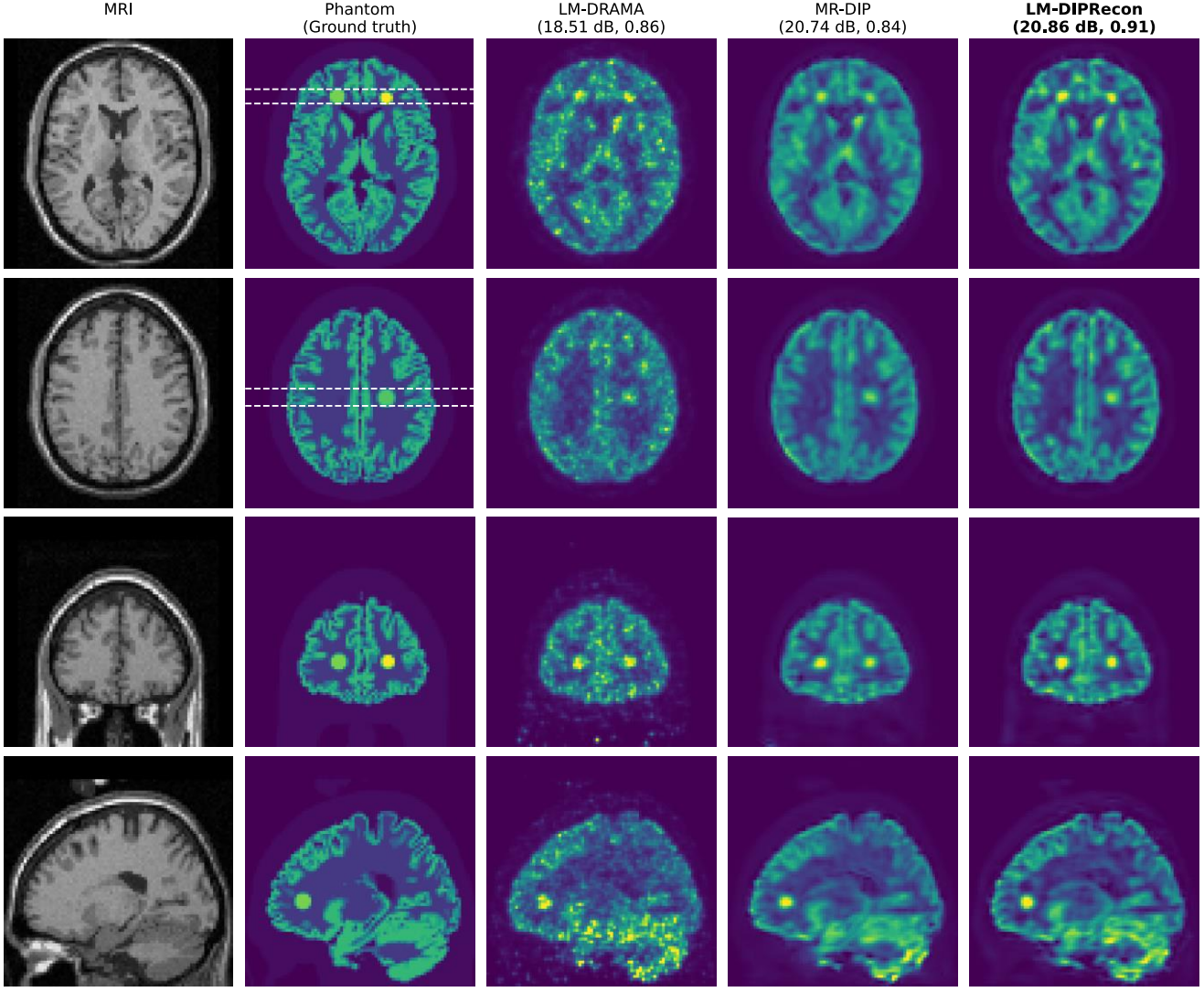


Fig. 2. Images of simulation data reconstructed by the proposed method and the other methods. From left to right, MRI and phantom image, LM-DRAMA, MR-DIP and LM-DIPRecon. Each image is tagged with its PSNR and CR. White dot lines indicate the position of profiles in Fig. 3.

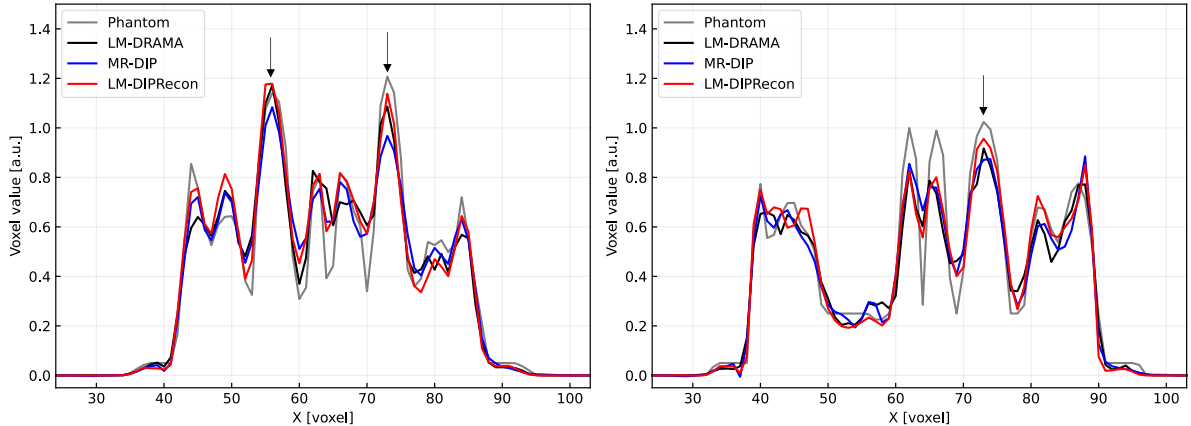


Fig. 3. Profiles on images of simulation data reconstructed by the proposed method and the other method. Left is a profile with six-pixel width across two small tumors, as indicated by the white dot lines on the first row of Fig. 2. Right is a profile with seven-pixel width across one large tumor, as indicated by the white dot lines on the second row of Fig. 2. Arrows indicate the position of the tumors.

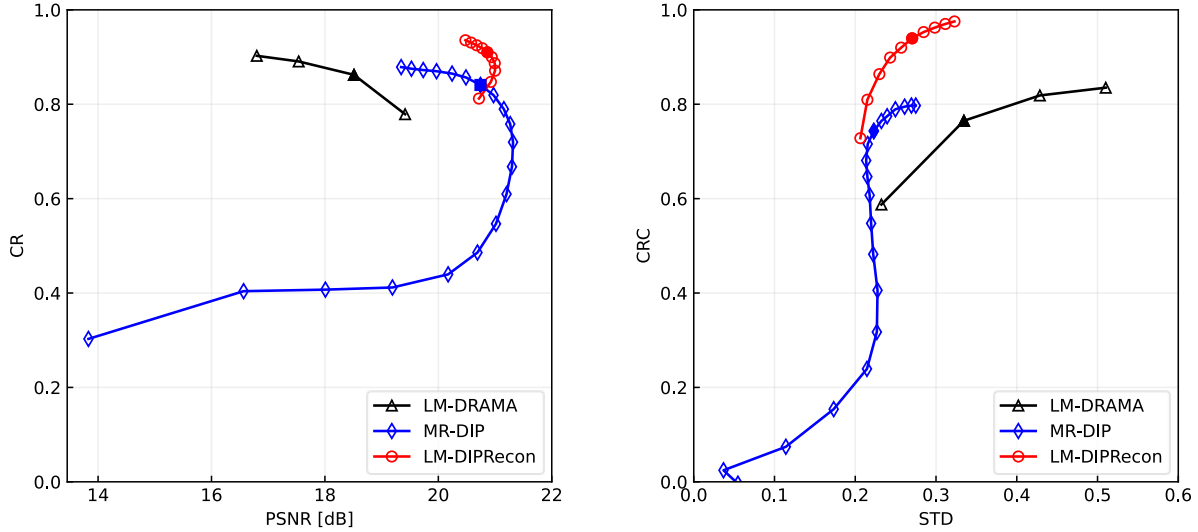


Fig. 4. Tradeoff curves between contrast and noise on the simulation study: CR versus PSNR (left) and CRC versus STD (right). Fill markers correspond to the images, as shown in Fig. 2. CR was calculated for the union of three tumor regions. CRC was calculated for the ROIs on the gray matter and tumor regions. STD was calculated for the ROIs on the white matter. The plots of LM-DRAMA correspond to 1, 2, 3, and 4 main-iterations. The plots of MR-DIP correspond to 100, 200, ..., 2000 epochs. The plots of LM-DIPRecon correspond to 20, 40,..., 200 iterations.

$$b_k = \frac{1}{N_{b,k}} \sum_{j \in R_{b,k}} x_j, \quad (28)$$

where $N_{a,k}$ is the number of voxels inside the k -th ROI on the GM and tumor, $N_{b,k}$ is the number of voxels inside the k -th ROI on the WM, $R_{a,k}$ is the k -th ROI on the GM and tumor, $R_{b,k}$ is the k -th ROI on the WM.

The STD can be calculated by the following equation.

$$\text{STD} = \frac{1}{\bar{b}} \sqrt{\frac{1}{K_b} \sum_{k=1}^{K_b} (b_k - \bar{b})^2}. \quad (29)$$

In this study, $K_a = 20$ for the GM, $K_a = 18$ for the tumor, and $K_b = 25$ for the WM.

In the clinical study, for ROI uptake quantification, the uptakes were calculated for the ROI on the thalamus. In addition, STD was calculated for the reconstructed images of clinical data.

In both simulation and clinical studies, we compared the following methods.

- **LM-DRAMA:** We performed the LM-DRAMA with 1, 2, 3, and 4 main-iterations. We applied 3D Gaussian filter with full-width-at-half-maximum of 3 mm as a post smoothing. For display, we chose the LM-DRAMA with two main-iteration because it is a default setting of the HITS-655000.
- **MR-DIP:** We performed the MR-DIP using the reconstructed image of LM-DRAMA with two main-

iteration, as the label. We used the Adam method and performed 2000 epochs at maximum.

- **LM-DIPRecon:** We performed the two-step approach as explained above. In the first step, we performed the MR-DIP using Adam method with 1000 epochs, where the label was the reconstructed image by one main-iteration of LM-DRAMA. The trained network by MR-DIP was used as the initial network parameter $\theta^{(0)}$. In the second step, we performed 200 iterations of Algorithm 1 at maximum.

V.RESULTS

Fig. 2 shows the images of simulation data reconstructed by the proposed method and the other methods. The images were tagged with their PSNRs and CRs. The reconstructed image of LM-DRAMA was noisy because the post smoothing was limited to 3 mm. Applying MR-DIP reduced the noise at a slight cost of the contrast. The LM-DIPRecon method maintained the contrast and provided sharper images than those of MR-DIP.

Fig. 3 shows the profiles across the tumor regions. The peaks of profile on MR-DIP at tumor positions tended to be lower than the phantom as shown in Fig. 3. The LM-DIPRecon obtained closer peaks to the phantom than the MR-DIP.

Fig. 4 shows the tradeoff curves between contrast and noise in the simulation study: CR vs. PSNR and CRC vs. STD. For the LM-DRAMA, the noise increased as the main-iteration increased. The MR-DIP improved the PSNR and STD relative to the LM-DRAMA, but the CR and CRC were lower than those of LM-DRAMA. The LM-DIPRecon maintained the same contrast as LM-DRAMA while improving PSNR and STD.

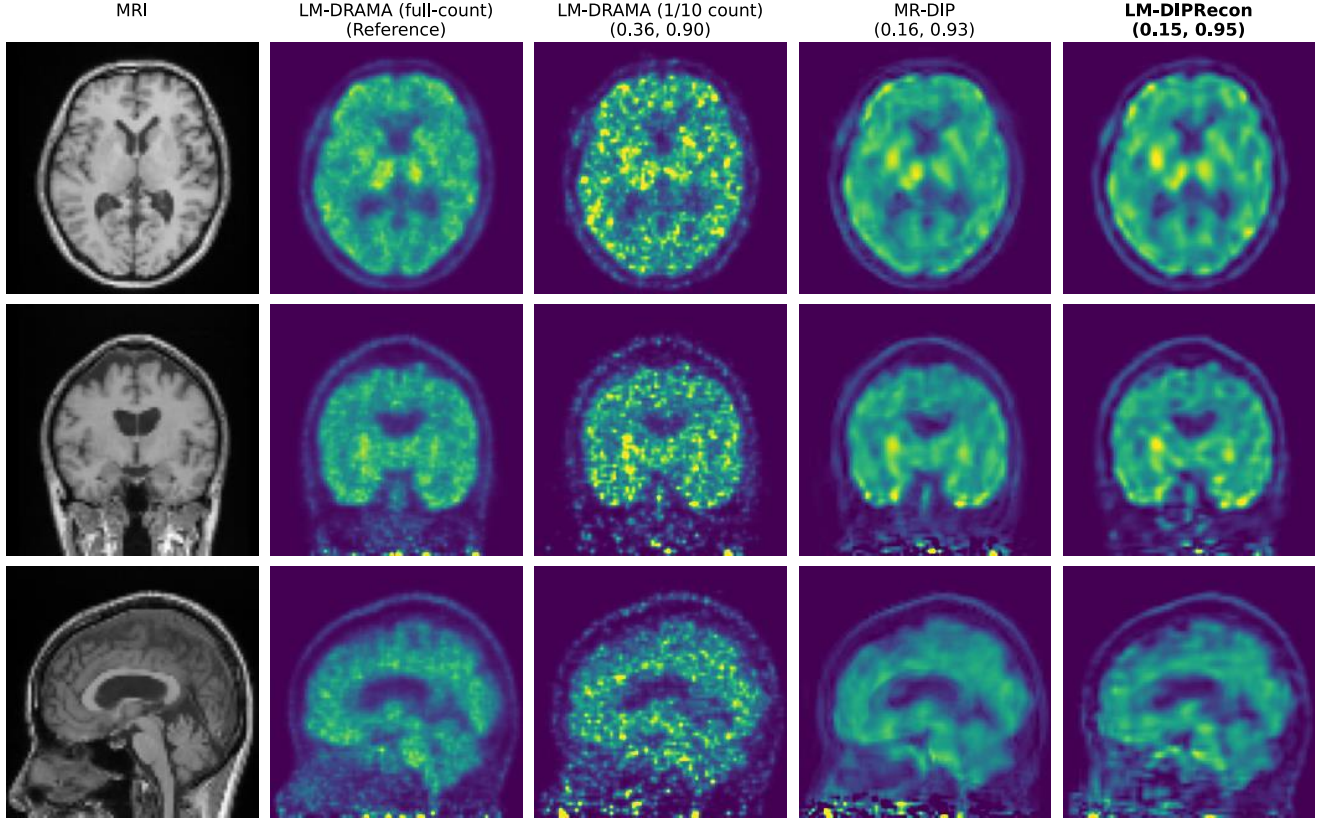


Fig. 5. Images of clinical data reconstructed by the proposed method and the other methods. From left to right, MRI, LM-DRAMA with full-count, LM-DRAMA with 1/10 count, MR-DIP and LM-DIPRecon. The images are tagged with the STD and the uptake.

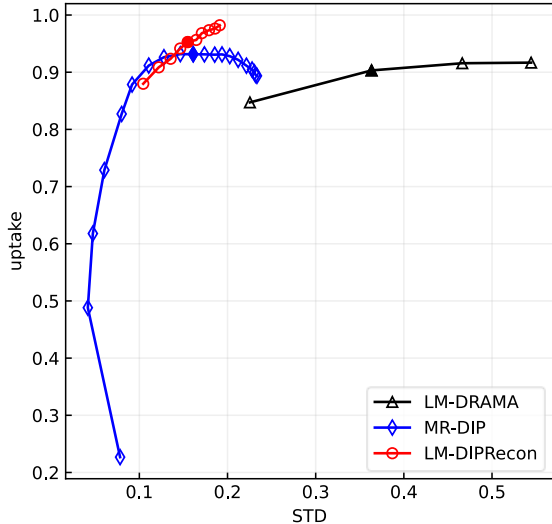


Fig. 6. Tradeoff curves between contrast and noise on the clinical study: Uptake versus STD. Fill markers correspond to the images as shown in Fig. 5. Uptake was calculated for the ROI on the thalamus. STD was calculated for the ROIs on the white matter. The plots of LM-DRAMA correspond to 1, 2, 3, and 4 main-iterations. The plots of MR-DIP correspond to 100, 200, ..., 2000 epochs. The plots of LM-DIPRecon correspond to 20, 40, ..., 200 iterations.

Fig. 5 shows the images of clinical data reconstructed by the proposed method and the other methods. The images showed that the ^{11}C -MeQAA accumulated in the thalamus [34]. Although the reconstructed images at 1/10 count were very noisy, both MR-DIP and LM-DIPRecon reduced the noises. In addition, LM-DIPRecon restored the gray matter structure more clearly than MR-DIP.

Fig. 6 shows the tradeoff curves between contrast and noise in the clinical study: Uptake vs. STD. The LM-DIPRecon provided a higher uptake than those of the other methods.

VI. DISCUSSION

In this study, we incorporated DIP into list-mode PET image reconstruction using an ADMM framework. As the computation efficiency of list-mode PET image reconstruction depends on the number of events not on the number of LORs, the proposed LM-DIPRecon method will be suitable for a PET scanner with many LORs and additional information such as TOF and DOI.

In the simulation study, LM-DIPRecon provided sharper images visually than those of MR-DIP (Fig 2). This is because the number of iterations of list-mode PET image reconstruction in LM-DIPRecon is virtually larger than that of MR-DIP. The MR-DIP train a CNN to map an MR image to a PET image reconstructed using LM-DRAMA with two main-iterations. Therefore, the degree of convergence of the MR-DIP image to

the maximum likelihood solution is limited to the level of two main-iterations. On the other hand, LM-DIPRecon performs more iterations of regularized LM-DRAMA through solving subproblem (10). For example, $N = 200$ and $M_1 = 2$ corresponds to 10 main-iterations with 40 subsets. Hence, the LM-DIPRecon method could reconstruct a more convergent image than the MR-DIP within the constraint that the image is representable by the CNN. This is a reason why the images of LM-DIPRecon were sharper than those of MR-DIP.

The LM-DIPRecon method provided better tradeoff curves between contrast and noise than those of the other methods (Fig. 4). However, in some cases, the tradeoff curves of LM-DIPRecon and MR-DIP overlapped (Fig 4. Left). When the computation time is prioritized, MR-DIP may become the preferred option instead of LM-DIPRecon. However, the merit of LM-DIPRecon is consistency with measured data. The MR-DIP method can be consistent with label image, but the consistency with the measured data is limited by the label image in principle. Hence, the risk of eliminating the signal such as tumor by the non-linear image processing such as MR-DIP may be reduced by the LM-DIPRecon. When the data consistency is prioritized, the LM-DIPRecon is recommended.

In the clinical study, LM-DIPRecon visualized a clearer structure of GM than MR-DIP (Fig. 5). The image quality of real data depends on factors such as an imperfection of data correction or a subject motion. Note that these factors degrade the image quality and may make the visual difference between the reconstruction methods small. The LM-DIPRecon method provided a better tradeoff curve of uptake vs STD than the other methods, similar to the simulation study (Fig. 6). As the reconstructed image of LM-DRAMA had been noisy even at full count, we tried to apply the MR-DIP and LM-DIPRecon methods to the clinical data having the full count. Although both MR-DIP and LM-DIPRecon provided less noisy images than LM-DRAMA, the LM-DIPRecon method visualized a slightly finer structure of GM than MR-DIP (see supplemental material). Although the true image is unknown in the clinical study, the LM-DIPRecon showed the potential to be useful for the clinical study.

Currently, the number of LORs of research tomographs have achieved the order of 10^9 . For example, the number of LORs of uEXPLORER total body PET/CT scanner is 92×10^9 [36]. In addition, the number of LORs of HITS-655000 brain PET scanner with 4-layer DOI detectors which was used in this study is 120×10^9 [34]. To full-use of the measured information in these scanners, the list-mode PET image reconstruction is still needed. The simulation and clinical results of the brain PET scanner with DOI detectors demonstrated the feasibility of the LM-DIPRecon for the PET scanners with a large number of LORs.

The limitation of the LM-DIPRecon is a long computation time. In this study, the regularized LM-DRAMA was computed using 6 cores of Intel i7-5930k 3.5GHz through the message passing interface, and the MR-DIP was computed using NVIDIA Quadro P6000 graphics card. In this condition, the two sub-iterations of regularized LM-DRAMA took 2-3 seconds, and the ten sub-iterations of L-BFGS method for the MR-DIP took about 96 seconds. Hence, 200 iterations of LM-DIPRecon took about 2×10^4 seconds in our environment. As the computational cost of MR-DIP was higher than regularized

LM-DRAMA, we could reduce the total computational cost by increasing the number of sub-iterations of the regularized LM-DRAMA and decreasing the number of iterations of the LM-DIPRecon. However, as the computational cost of the regularized LM-DRAMA is dependent on the number of events, the best balance between the sub-iteration number of LM-DRAMA and the number of iterations of LM-DIPRecon cannot be determined uniquely.

In the future, an extension of LM-DIPRecon to 4D image reconstruction [37], [38] can be considered. As list-mode data has finer temporal information than the dynamic sinograms, LM-4D-DIPRecon may be useful for dynamic PET imaging or direct parametric imaging [39]. The high temporal resolution of list data is also useful for motion correction [40], [41]. From these ideas, the LM-DIPRecon can be expected to be useful for the 4D and 5D problems involving dynamic imaging of moving organs [42]. In this study, the MR image was used as a prior distribution image of the DIP, but an MR-guided deep decoder (MR-GDD) [43] which uses the MR image through an attention mechanism has already been proposed. As the MR-GDD works to improve the contrast of the tumor which does not exist on the MR image, the list-mode PET image reconstruction using MR-GDD may improve the contrast of the tumor relative to the LM-DIPRecon.

VII. CONCLUSION

We proposed list-mode PET image reconstruction using DIP. We incorporated DIP into list-mode PET image reconstruction using an ADMM framework. We evaluated the proposed method using simulation and clinical data. The proposed method provided a sharper image, higher contrast, and lower noise than the other methods. These results indicated that the proposed method is promising for the next generation of brain PET scanners.

APPENDIX

In the experiments, data corrections [44] and shift-invariant point-spread-function (PSF) [45] were incorporated in the LM-DRAMA as,

$$\tilde{x}_{j,EM}^{(k,q+1)} = x_j^{(k,q)} + x_j^{(k,q)} \lambda^{(k,q)} \left(\frac{N_{\text{sub}}}{\tilde{S}_j} \sum_{j'} P_{jj'} \sum_{t \in \text{Sub}_q} \frac{a_{i(t)j'}}{\tilde{y}_{i(t)}^{(k,q)}} - 1 \right), \quad (30)$$

$$\tilde{x}_{j,EM}^{(k,q+1)} = \max(\tilde{x}_{j,EM}^{(k,q+1)}, 0), \quad (31)$$

$$\tilde{y}_i^{(k,q)} = A_i \left(\sum_j a_{ij} \sum_{j'} P_{jj'} x_{j'}^{(k,q)} \right) + \frac{C_i}{B_i}, \quad (32)$$

$$\tilde{S}_j = \sum_j P_{jj'} \sum_i B_i a_{ij'}, \quad (33)$$

$$A_i = e^{-\sum_j a_{ij} \mu_j}, \quad (34)$$

$$\delta(t) = \begin{cases} 1 & t \text{ is prompt} \\ -1 & t \text{ is delayed} \end{cases} \quad (35)$$

where A is an attenuation probability, B is an efficiency of LOR, C is a scatter component, P is a PSF, \tilde{S} is a sensitivity image including the LOR efficiency and the PSF, μ is an image of linear attenuation coefficient (μ -map), and δ is a sign of event for the random correction of the delayed subtraction.

The efficiency of LOR was estimated by the component-based normalization technique [46]. The scatter component was estimated by the single scatter simulation method [47]. In the simulation study, the μ -map of the phantom image was used for the attenuation correction (AC). In the clinical study, the μ -map was estimated by the segmentation of the reconstructed image without AC. The PSF was modeled by the 3-D Gaussian function with full-width at half-maximum of one voxel.

ACKNOWLEDGMENT

We thank the members of the 5th research group in the central research laboratory of the Hamamatsu Photonics K. K. for their kind support.

REFERENCES

- [1] M. E. Phelps, *PET: Molecular Imaging and Its Biological Applications*. New York, NY, USA: Springer-Verlag, 2004. [Online]. Available: <https://www.springer.com/la/book/9780387403595>
- [2] J. Qi *et al.*, “High-resolution 3D Bayesian image reconstruction using the microPET small-animal scanner,” *Phys. Med. Biol.*, vol. 43, no. 4, pp. 1001-1014, 1998.
- [3] J. Nuyts *et al.*, “A concave prior penalizing relative differences for maximum-a-posterior reconstruction in emission tomography,” *IEEE Trans. Nucl. Sci.*, vol. 49, no. 1, pp. 56-60, 2002.
- [4] G. Wang and J. Qi, “PET image reconstruction using kernel methods,” *IEEE Trans. Med. Imaging*, vol 34, no. 1, pp. 61-71, 2015.
- [5] B. Bai, Q. Li, R. M. Leahy, “Magnetic resonance-guided positron emission tomography image reconstruction,” *Semin. Nucl. Med.*, vol.43, no. 1, pp. 30-44, 2013.
- [6] C. Comtat *et al.*, “Clinically feasible reconstruction of 3D whole-body PET/CT data using blurred anatomical labels,” *Phys. Med. Biol.*, vol. 47, No. 1, pp. 1-20, 2002.
- [7] A. J. Reader *et al.*, “Deep learning for PET image reconstruction,” *IEEE Trans. Radiat. Plasma Med. Sci.*, vol. 5, no. 1, pp. 1-25, 2020.
- [8] K. Gong *et al.*, “The evolution of image reconstruction in PET: From filtered back-projection to artificial intelligence,” *PET Clin.*, vol. 16, no. 4, pp. 533-542, 2021.
- [9] A. Mehranian and A. J. Reader, “Model-based deep learning PET image reconstruction using forward-backward splitting expectation-maximization,” *IEEE Trans. Radiat. Plasma Med. Sci.*, vol. 5, no. 1, pp. 54-64, 2020.
- [10] K. Ote and F. Hashimoto, “Deep-learning-based fast TOF-PET image reconstruction using direction information,” *Radiol. Phys. Technol.*, vol. 15, pp. 72-82, 2022.
- [11] B. Zhu *et al.*, “Image reconstruction by domain-transform manifold learning,” *Nature*, vol. 555, no. 7697, pp. 487-492, 2018.
- [12] W. Whiteley, W. K. Luk, and J. Gregor, “DirectPET: full-size neural network PET reconstruction from sinogram data,” *J. Med. Imaging*, vol. 7, no. 3, 032503, 2020.
- [13] I. Häggström *et al.*, “DeepPET: A deep encoder-decoder network for directly solving the PET image reconstruction inverse problem,” *Med. Image Anal.*, vol. 54, pp. 253–262, 2019.
- [14] K. Gong *et al.*, “Iterative PET image reconstruction using convolutional neural network representation,” *IEEE Trans. Med. Imaging*, vol. 38, no. 3, pp. 675-685, 2018.
- [15] D. Ulyanov, A. Vedaldi and V. Lempitsky, “Deep image prior,” *Int. J. Comput. Vis.*, vol. 128, pp. 1867-1888, 2020.
- [16] K. Gong *et al.*, “PET image reconstruction using deep image prior,” *IEEE Trans. Med. Imaging*, vol. 38, no. 7, pp. 1655-1665, 2018.
- [17] T. Yokota *et al.*, “Dynamic PET image reconstruction using non-negative matrix factorization incorporated with deep image prior,” In *2019 IEEE/CVF International Conference on Computer Vision (ICCV)*, Seoul, Korea, pp. 3126-3135, 2020.
- [18] F. Hashimoto, K. Ote, and Y. Onishi, “PET image reconstruction incorporating deep image prior and a forward projection model,” *IEEE Trans. Radiat. Plasma Med. Sci.*, Early Access, 2022. 10.1109/TRPMS.2022.3161569
- [19] M. G. Spangler-Bickell *et al.*, “Ultra-fast list-mode reconstruction of short PET frames and example applications,” *J. Nucl. Med.*, vol. 62, no. 2, pp. 287-292, 2021.
- [20] S. Boyd *et al.*, “Distributed optimization and statistical learning via the alternating direction method of multipliers,” *Found. Trends Mach. Learn.*, vol. 3, no. 1, pp. 1-122, 2011.
- [21] X. Cao, Q. Xie, and P. Xiao, “A regularized relaxed ordered subset list-mode reconstruction algorithm and its preliminary application to undersampling PET imaging,” *Phys. Med. Biol.*, vol. 60, no. 1, pp. 49-66, 2015.
- [22] T. Nakayam and H. Kudo, “Derivation and implementation of ordered-subsets algorithms for list-mode PET data,” *2005 IEEE Nucl. Sci. Symp. Conf. Rec.*, Fajardo, PR, USA, pp. 1950-1954, 2005.
- [23] E. Tanaka and H. Kudo, “Subset-dependent relaxation in block iterative algorithms for image reconstruction in emission tomography,” *Phys. Med. Biol.*, vol. 48, no. 10, 1405-1422, 2003.
- [24] J. Qi, “Calculation of the sensitivity image in list-mode reconstruction for PET,” *IEEE Trans. Nucl. Sci.*, vol. 53, no. 5, pp. 2746-2751, 2006.
- [25] J. Cui *et al.*, “PET image denoising using unsupervised deep learning,” *Eur. J. Nucl. Med. Mol. Imaging*, vol. 46, no. 13, pp. 2780-2789, 2019.
- [26] F. Hashimoto *et al.*, “Dynamic PET image denoising using deep convolutional neural networks without prior training datasets,” *IEEE Access*, vol. 7, pp. 96594-96603, 2019.
- [27] K. Lange, D. R. Hunter, and I. Yang, “Optimization transfer using surrogate objective functions,” *J. Comput. Graph. Stat.*, vol. 9, no. 1, pp. 1-20, 2000.
- [28] G. Wang and J. Qi, “Penalized likelihood PET image reconstruction using patch-based edge-preserving regularization,” *IEEE Trans. Med. Imaging*, vol. 31, no. 12, pp. 2194-2204, 2012.
- [29] E. S. Helou Neto and A. R. De Pierro, “Convergence results for scaled gradient algorithms in positron emission tomography,” *Inverse Problems*, vol. 21, no. 6, pp. 1905-1914, 2005.
- [30] Ö. Çiçek *et al.*, “3D U-Net: learning dense volumetric segmentation from sparse annotation,” *Medical Image Computing and Computer Assisted Intervention (MICCAI)*, LNCS, vol. 9901, pp. 424-432, 2016.
- [31] R. Pascanu, T. Mikolov, and Y. Bengio, “On the difficulty of training recurrent neural networks,” *arXiv preprint arXiv: 1211.5063*, 2013
- [32] D. P. Kingma and J. Ba, “Adam: a method of stochastic optimization,” *arXiv preprint arXiv: 1412.6980*, 2017
- [33] D. L. Collins *et al.*, “Design and construction of a realistic digital brain phantom,” *IEEE Trans Med. Imaging*, vol. 17, no. 3, pp. 463-468, 1998.
- [34] M. Watanabe *et al.*, “Performance evaluation of a high-resolution brain PET scanner using four-layer MPPC DOI detectors,” *Phys. Med. Biol.*, vol. 62, no. 17, pp. 7148-7166, 2017.
- [35] K. Nakaizumi *et al.*, “In vivo depiction of $\alpha 7$ nicotinic receptor loss for cognitive decline in Alzheimer’s disease,” *J. Alzheimers Dis.*, vol. 61, no. 4, pp. 1355-1365.
- [36] B. A. Spencer *et al.*, “Performance evaluation of the uEXPLORER total-body PET/CT scanner based on NEMA NU 2-2018 with additional tests to characterize PET scanners with a long axial field of view,” *J. Nucl. Med.*, vol. 62, no. 6, pp. 861-870, 2021.
- [37] A. J. Reader and J. Verhaeghe, “4D image reconstruction for emission tomography,” *Phys. Med. Biol.*, vol. 59, no. 22, R371-R418, 2014.
- [38] F. Hashimoto *et al.*, “4D deep image prior: dynamic PET image denoising using an unsupervised four-dimensional branch convolutional neural network,” *Phys. Med. Biol.*, vol. 66, no. 1, pp. 015006, 2021.
- [39] G. Wang *et al.*, “PET parametric imaging: past, present, and future,” *IEEE Trans. Radiat. Plasma Med. Sci.*, vol. 4, no. 6, pp. 663-675, 2020.
- [40] A. Rahimim *et al.*, “Motion compensation in histogram-mode and list-mode EM reconstructions: beyond the event-driven approach,” *IEEE Trans. Nucl. Sci.*, vol. 51, no. 5, pp. 2588-2596, 2004.
- [41] R. E. Carson *et al.*, “Design of a motion-compensation OSEM list-mode algorithm for resolution-recovery reconstruction for the HRRT,” *2003 IEEE Nucl. Sci. Symp. Conf. Rec.*, Portland, OR, USA, pp. 3281-3285, 2004.
- [42] M. Defrise and G. T. Gullberg, “Image reconstruction,” *Phys. Med. Biol.*, vol. 51, no. 13, R139-154, 2006.
- [43] Y. Onishi *et al.*, “Anatomical-guided attention enhances unsupervised PET image denoising performance,” *Med. Image Anal.*, vol. 74, 102226, 2021.

- [44] A. Rahmim *et al.*, “Statistical dynamic image reconstruction in state-of-the-art high resolution PET,” *Phys. Med. Biol.* vol. 50, no. 20, pp. 4887-4912, 2005.
- [45] A. J. Reader *et al.*, “One-pass list-mode EM algorithm for high-resolution 3-D PET image reconstruction into large arrays,” *IEEE Trans. Nucl. Sci.*, vol. 49, no. 3, pp. 693-699, 2002.
- [46] R. D. Badawi and P. K. Marsden, “Developments in component-based normalization for 3D PET,” *Phys. Med. Biol.*, vol. 44, no. 2, pp. 571-594, 1999.
- [47] C. C. Watson, “New, faster, image-based scatter correction for 3D PET,” *IEEE Trans. Nucl. Sci.*, vol. 47, no. 4, pp. 1587-1594, 2000.